Available online at www.sciencedirect.com
ScienceDirect
Computational Materials Science xxx (2007) xxx–xxx
COMPUTATIONAL MATERIALS SCIENCE
www.elsevier.com/locate/commatsci

Computational modelling of thermal impact welded PEEK/steel single lap tensile specimens

Johannes Utzinger [a,*], Martin Bos [b], Martin Floeck [c], Andreas Menzel [a], Ellen Kuhl [a], Rainer Renz [b], Klaus Friedrich [c], Alois K. Schlarb [c], Paul Steinmann [a]

[a] Chair of Applied Mechanics, University of Kaiserslautern, P.O. Box 3049, D-67653 Kaiserslautern, Germany
[b] Lehrstuhl für Ressourcengerechte Produktentwicklung, University of Kaiserslautern, P.O. Box 3049, D-67653 Kaiserslautern, Germany
[c] Institut für Verbundwerkstoffe GmbH, Erwin-Schrödinger-Straße, Gebäude 58, D-67663 Kaiserslautern, Germany

Received 13 November 2006; accepted 20 April 2007

Abstract

In this contribution, an interfacial traction-separation-law based on elastoplasticity with Lemaitre-type-damage is applied. Related constitutive equations are decoupled with respect to a local orthonormal frame such that the stress–strain response is controlled independently in these directions. The constitutive traction-separation-law is applied to the simulation of thermal impact welded (TIW) single lap tensile specimens. The specimens consist of two steel substrates and a PEEK foil which is laid in between the joining zone. Tensile tests and electronic speckle pattern interferometry (ESPI) are consulted to verify the simulations. To provide brief background information, a short review on the manufacturing method of TIW and the method of ESPI is included.

The comparisons of measurements and computations show that one-dimensional integral data given by global force–displacement-curves can be simulated sufficiently accurate. Two-dimensional data given by displacement and strain fields reveal good similarities between measurements and computations.

PACS: 02.70.Dh; 46.15.−x; 46.35.+z; 81.05.Qk; 81.20.Vj; 81.70.Fy

Keywords: Interface; Traction-separation-law; Finite Element Method; Composites; Welding; Electronic Speckle Pattern Interferometry

1. Introduction

Since fibre-reinforced thermoplastic materials offer a great potential for lightweight design and construction, they are increasing in use. They feature high specific stiffness, strength, and impact resistance as well as an excellent resistance against many chemical agents. Furthermore, many polymeric composite materials exhibit very good tribological properties, i.e. a low wear rate and low coefficients of friction [1–4]. However, the limits of today's composites can be pushed even further by combining their advantages with the properties of traditional construction materials, e.g. thermal conductivity or strength. Moreover, the use of composite materials in more and more applications requires reliable, strong and easy-to-use methods of joining metal parts with composite structures. Thus, the development of new joining techniques for metals and thermoplastic polymeric resins is of paramount importance for the evolution of this active field of research.

Amongst others, thermal impact welding (TIW) is a novel technique for joining thermoplastics with steel. Since poly(-ether-ether)-ketone (PEEK) is a heavy-duty industrial thermoplastic resin, which is widely used in sophisticated applications, the suitability of the TIW-process needs to be verified for this kind of polymeric compound. PEEK seems to be a particularly interesting polymer

* Corresponding author. Tel.: +49 631 205 3855; fax: +49 631 205 2128.
E-mail address: utzinger@rhrk.uni-kl.de (J. Utzinger).
URL: http://mechanik.mv.uni-kl.de (J. Utzinger).

0927-0256/$ - see front matter © 2007 Elsevier B.V. All rights reserved.
doi:10.1016/j.commatsci.2007.04.015

because its mechanical and thermal properties are in the upper range compared to other commercially available polymeric materials [5]. Preliminary tests proved that TIW can be employed for joining PEEK with metal substrates.

Developing a new joining method necessitates the thorough investigation of the stability and reproducibility of the process. At the same time, it must be ensured that the manufactured components are free of flaws. Few reports concerning a hot press process for joining thermoplastics with metals can be found in the technical literature. Two of those rare papers are [6,7]. Oster et al. [6] describe how a hot press process (i.e. thermal impact welding) can be employed for manufacturing flat samples for tribological experiments. The results of the preliminary experiments performed prior to the main work described in the first part of this paper are in good accordance with the findings in [6,7].

Simultaneously, adequate simulation techniques are investigated, which constitute the main objective of the present paper: the appropriate computational modelling of the loading of thermal impact welded specimens in order to predict the mechanical properties of more complex PEEK-steel components manufactured with TIW.

Using the Finite Element Method (FEM) for simulations, the importance of so-called interface elements must be emphasised. The representation of the loading behaviour of the weld interface is essentially based on appropriate material models for the interface elements. In this context, it is the long term objective to develop a reliable simulation tool for thermal impact welded PEEK-steel components.

A first step is the phenomenological modelling of single lap tensile specimens. For this purpose, specimens have been manufactured using a bench-scale hot press; they have subsequently been tested in a tensile test rig, recording both the tensile strength and the in-plane and out-of-plane deformation using modern optical measurement techniques based on Electronic Speckle Pattern Interferometry [8]. The resulting empirical data has been used to validate the FEM-based numerical modelling.

As such, the developed models shall permit the determination of the strength and inelastic properties of the joint so that the number of experiments can be reduced.

The paper is organised as follows: first, an overview on the thermal impact welding technique is given in Section 2.1. Next, a short outline on electronic speckle pattern interferometry (ESPI) is highlighted in Section 2.2. ESPI is used to obtain locally resolved displacement and strain fields. Then, aspects of the applied material law, namely elastoplasticity coupled with Lemaitre-type-damage, which successfully serves for phenomenological simulations of the interface problem at hand, are stated in detail in Section 3. Section 4 focuses on the numerical treatment of the interface elements embedded into a FEM context, followed by the demonstration of numerical results which are compared to experimental data in Section 5. Conclusions are summarised in Section 6.

2. Manufacturing and strain analysis

2.1. Manufacturing

The material used for the investigations in the present paper is on the one hand a PEEK-based polymer-compound. On the other hand, a low carbon steel was used as metallic counterpart.

PEEK is a semi-crystalline thermoplastic. Its melting temperature is 334 °C; the glass transition temperature is 143 °C. The maximum continuous utilisation temperature of PEEK is 260 °C. Furthermore, PEEK features a high specific stiffness and strength, an excellent resistance to chemical agents and can exhibit a maximum degree of crystallinity of 48%. The compound used in this study is reinforced with an amount of 10 wt% short carbon fibres. Moreover, a total of approx. 20 wt% of various micro-particles (graphite and PTFE) were added to the formulation of the compound to improve the mechanical properties.

The mild steel DC01 (German standard, also referred to as DIN EN 10131 or material number 1.0330) exhibits a Young's modulus E of approximately 165 GPa, a yield strength $R_{p0.2}$ of 145 MPa, and a tensile strength R_m of approximately 290 MPa. The steel substrates were grit-blasted before having been thermally welded. Fig. 1 shows the surface of the blasted specimens. The mean surface roughness index after blasting is 2.71 μm, compared to

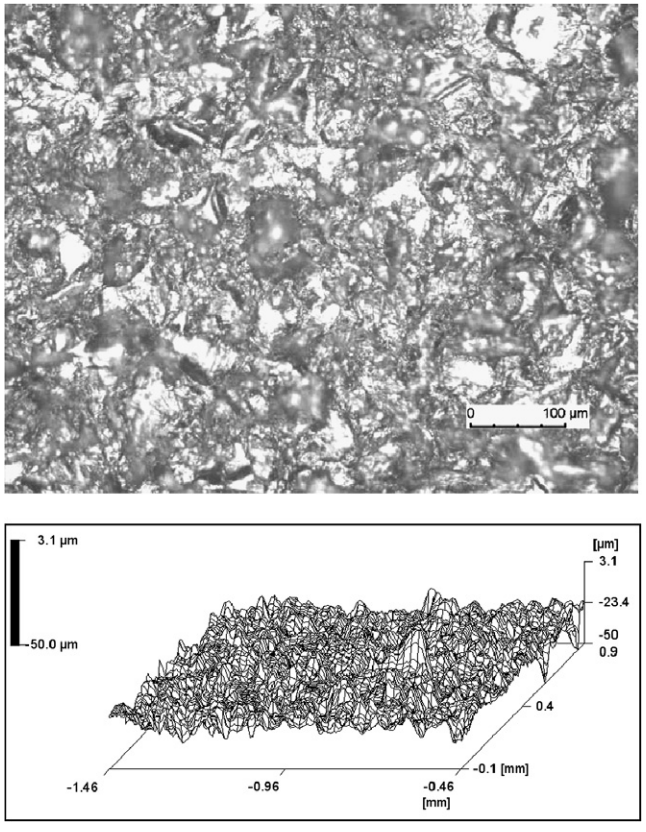

Fig. 1. Light microscopic image of the blasted surface (top) and laser profilometric scan (bottom).

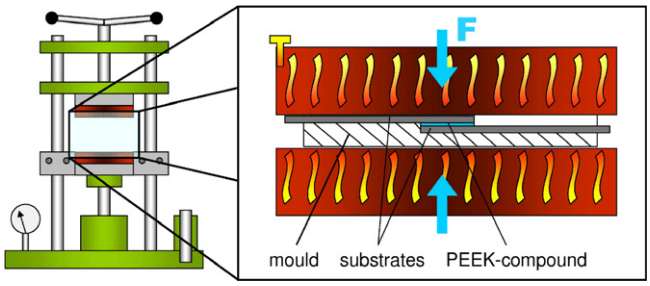

Fig. 2. Schematic representation of the hot press process.

0.67 μm in case of the unfinished surface. It is believed that the enhanced surface roughness after grit-blasting facilitates the bonding of the polymeric compound to the metal substrate due to mechanical hooking of the polymer. Furthermore, blasting leads to a chemical activation of the surface layer, thus ameliorating the adhesion between the two materials to be joined.

In order to manufacture the tensile samples, a joining technique called thermal impact welding (TIW) was employed. TIW is a process in which the metallic substrates together with a PEEK-layer are inserted into a hot press, see Fig. 2. The parts to be joined are then heated to 380 °C, a temperature above the melting temperature of the PEEK-compound. Once the PEEK has melted, a pressure is applied to the setup and the heating of the hot press is switched off. As the temperature drops, the PEEK becomes more and more viscous. During this process, the pressure on the parts to be joined needs to be maintained, because a decrease in joining pressure could result in cavities or shrink holes in the polymer, thus leading to a reduced strength of the PEEK-layer and weak bonding to the metal substrates. Shortly before the PEEK eventually solidifies, the pressure needs to be increased in order to compensate the shrinkage due to crystallisation of the polymer. The specimens remain in the hot press until the temperature of the set-up drops below 300 °C to make sure that the polymeric compound solidifies and the removal of the still hot specimens does not influence the strength of the weld. The resulting samples were then tested using a tensile testing machine (model Zwick 1454-100/03) in order to produce force–displacement-curves. The sample geometry and the test set-up are displayed in Fig. 3. The single lap shear samples are mounted into the chuck jaw of the tensile testing machine. The tests were conducted at a constant cross head speed of 1 mm/min. During the tests, a data acquisition programme continuously recorded the tensile forces, the elongation, the displacement of the lower crosshead and the time. Taking the geometry of the samples in consideration, the averaged shear stress in the welded zone can be calculated.

2.2. Displacement and strain analysis

To specify the theoretical model it is necessary to compare not only force–displacement-curves. For a more

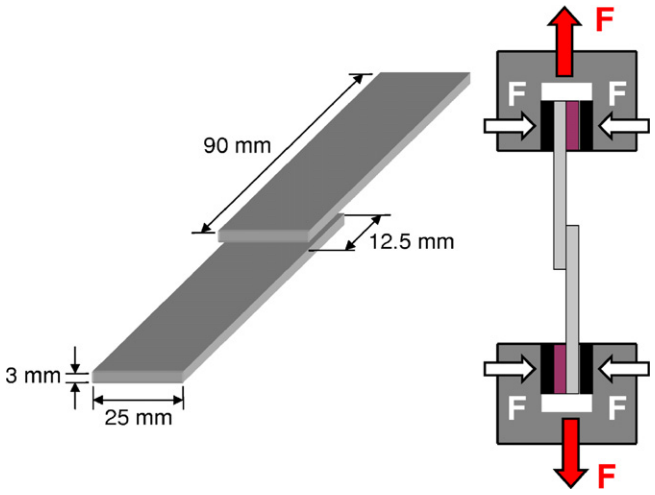

Fig. 3. Sample geometry (left) and test set-up (right).

detailed verification of the simulated single lap tensile specimens, a locally resolved optical measurement method is needed to obtain displacement and strain fields. Using the Electronic Speckle Pattern Interferometry (ESPI) it is possible to get this for all three dimensions and for different loadings. ESPI (Fig. 4) uses a laser which is split into a reference beam and a beam for the purpose of object illumination. After the recombination of the two beams the SPECKLE pattern (Fig. 5) is obtained that correlates with the roughness of the observed object. The phase Φ between the two laser beams depends on the optical path lengths. Deformation of the object changes this length and correlating pictures before and after loading enables the elimination of the unknown phase Φ. The result is the phase angle Δ which directly corresponds the deformation of the object. The accuracy of the measured phase angle depends only on the geometrical setup and the wavelength of the laser used. The achieved sensitivity based on a Q300 ESPI system by Dantec Ettemeyer [9] was better then 0.1 μm in all directions. Computing the gradient in space

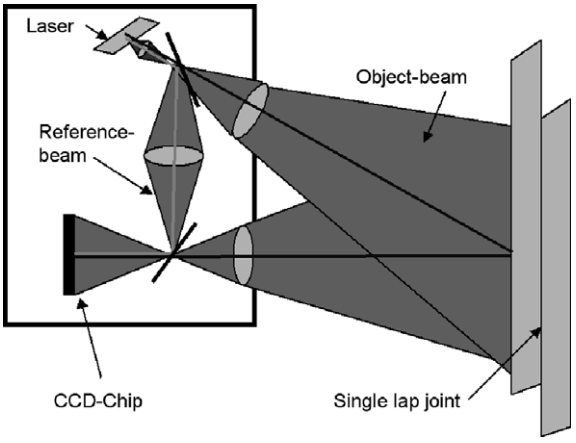

Fig. 4. Principle of ESPI.

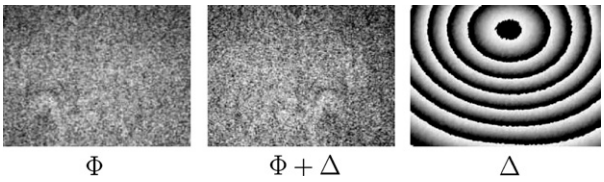

Fig. 5. SPECKLE pattern of a circular loaded plate.

of the displacement field determines the strain contribution in every point of the object.

3. Interfacial material model

It is the goal of this study to phenomenologically simulate shear tension tests of thermal impact welded metal/fibre–plastic composites. In this context, the finite element method is applied. For an appropriate modelling, the steel substrates are represented by continuum elements whereas the interface is modelled by so-called interface elements [10,11].

The mechanical relation between the bulk continuum and the interface is given by Cauchy's Lemma

$$\boldsymbol{\tau}(\boldsymbol{x}, -\boldsymbol{n}) = -\boldsymbol{\tau}(\boldsymbol{x}, \boldsymbol{n}) \tag{1}$$

and Cauchy's Theorem.

$$\boldsymbol{\tau} = \boldsymbol{\sigma} \cdot \boldsymbol{n} \tag{2}$$

By this, the orientation of the interface (in three dimensions treated as a surface) is taken into account; see Fig. 6 for an illustration. Here, $\boldsymbol{\tau}$ is the traction vector in the interface, $\boldsymbol{\sigma}$ is the continuum stress tensor for small strains and $\boldsymbol{n}$ is the normal vector of the interface and member of the orthonormal basis $\{\boldsymbol{s},\boldsymbol{t},\boldsymbol{n}\}$. The material behaviour of the interface itself is characterised by a so-called traction-separation-law so that the traction vector $\boldsymbol{\tau}$ in the interface is related to the relative displacement vector $\boldsymbol{v} = [\![\boldsymbol{u}]\!]$ of the interface edges.

Nevertheless, for the sake of units, a band width b is introduced [12] which appears in the so-called tangent operator $\boldsymbol{E}$ and takes the interpretation as a characteristic length. To reduce the number of parameters, the value of the band width b is set as 1.0 such that only the unit of b (length) becomes relevant. The orthonormal basis $\{\boldsymbol{s},\boldsymbol{t},\boldsymbol{n}\}$ is a locally defined quantity and generally moves with the interface. Here, only small displacements are taken into account – the initial configuration is consequently fixed for a geometrically linear analysis.

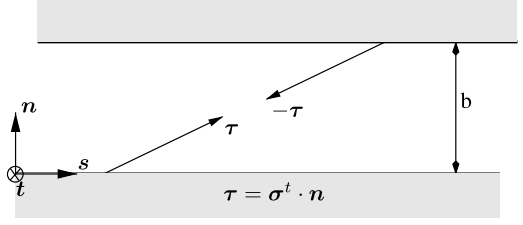

Fig. 6. Bulk continuum and embedded interface.

3.1. Elasticity

The elastic properties of the interface are supposed to be decoupled with respect to the local base system.

$$\boldsymbol{E}^{\mathrm{el}} = \boldsymbol{E}_s + \boldsymbol{E}_t + \boldsymbol{E}_n \quad \text{with} \tag{3}$$

$$\boldsymbol{E}_s = c_s\ \boldsymbol{s} \otimes \boldsymbol{s}, \quad \boldsymbol{E}_t = c_t\ \boldsymbol{t} \otimes \boldsymbol{t}, \quad \boldsymbol{E}_n = c_n\ \boldsymbol{n} \otimes \boldsymbol{n} \tag{4}$$

The elastic constants c_s, c_t, c_n constitute stiffness parameters according to the base directions. In the purely elastic case, the traction vector is computed via

$$\boldsymbol{\tau} = \boldsymbol{E}^{\mathrm{el}} \cdot \boldsymbol{v} \tag{5}$$

3.2. Elastoplasticity with damage

Next, the material model is extended to elastoplastic behaviour coupled with Lemaitre-type-damage. By this, accurate phenomenological simulations can be realised. The phenomenological Lemaitre-type-damage approach [13–15] relays on the idea that the load capacity of the specimen is related to the effective cross-sectional area or rather effective volume. This is expressed by means of the damage parameter $d \in [0,1]$. If $d = 1$, the material is fully damaged. With respect to the local base system $\{\boldsymbol{s},\boldsymbol{t},\boldsymbol{n}\}$, three different damage parameters $\boldsymbol{d} = (d_s, d_t, d_n)^t$ are distinguished.

For the sake of abbreviation, elements of $\{\boldsymbol{s},\boldsymbol{t},\boldsymbol{n}\}$ will in the following be represented by $\boldsymbol{i}$ if needed.

For elastoplasticity with damage, the traction vector is derived from a free energy function introduced as the sum of macroscopic and microscopic related contributions.

$$\Psi = \Psi_{\mathrm{macro}}(\boldsymbol{v}^{\mathrm{e}}) + \Psi_{\mathrm{micro}}(\boldsymbol{\alpha}) \quad \text{with} \tag{6}$$

$$\Psi_{\mathrm{macro}}(\boldsymbol{v}^{\mathrm{e}}) = \frac{1}{2}\boldsymbol{v}^{\mathrm{e}} \cdot [[1-d_s]\boldsymbol{E}_s + [1-d_t]\boldsymbol{E}_t + [1-d_n]\boldsymbol{E}_n] \cdot \boldsymbol{v}^{\mathrm{e}} \tag{7}$$

$$\Psi_{\mathrm{micro}}(\alpha) = \frac{1}{2}[H_s\alpha_s^2 + H_t\alpha_t^2 + H_n\alpha_n^2] \tag{8}$$

The elastic part of the relative displacement $\boldsymbol{v}^{\mathrm{e}}$ thereby represents the difference of the general relative displacement $\boldsymbol{v}$ and the plastic part of the relative displacement $\boldsymbol{v}^{\mathrm{p}}$, i.e. $\boldsymbol{v} = \boldsymbol{v}^{\mathrm{e}} + \boldsymbol{v}^{\mathrm{p}}$. Microscopic parts of the free energy which depend on the hardening moduli $\boldsymbol{H} = (H_s, H_t, H_n)^t$ and the plastic parameters $\boldsymbol{\alpha} = (\alpha_s, \alpha_t, \alpha_n)^t$ are not directly relevant for the traction vector which is derived from a hyperelastic format.

$$\frac{\partial \Psi}{\partial \boldsymbol{v}^{\mathrm{e}}} = [[1-d_s]\boldsymbol{E}_s + [1-d_t]\boldsymbol{E}_t + [1-d_n]\boldsymbol{E}_n] \cdot [\boldsymbol{v} - \boldsymbol{v}^{\mathrm{p}}] = \boldsymbol{\tau} \tag{9}$$

In view of the inelasticity framework subsequently elaborated, we next introduce so-called effective tractions related to the remaining undamaged portion of the material, namely

$$\bar{\boldsymbol{\tau}} = [\boldsymbol{E}_s + \boldsymbol{E}_t + \boldsymbol{E}_n] \cdot [\boldsymbol{v} - \boldsymbol{v}^{\mathrm{p}}] \tag{10}$$

Accordingly, this effective quantity serves as the main argument entering the yield functions which determine whether the actual state of deformation is admissible or not. With initial thresholds Y_{0s}, Y_{0t}, Y_{0n}, the yield functions Φ_s, Φ_t, Φ_n are introduced as

$$\Phi_i = |\bar{\boldsymbol{\tau}} \cdot \boldsymbol{i}| - [Y_{0i} - R_i] \leqslant 0 \tag{11}$$

wherein

$$R_i = -H_i \alpha_i \tag{12}$$

represent hardening stresses. A decoupled evolution equation is proposed as

$$\dot{\boldsymbol{v}}^{\mathrm{p}} = \dot{\boldsymbol{v}}_s^{\mathrm{p}} + \dot{\boldsymbol{v}}_t^{\mathrm{p}} + \dot{\boldsymbol{v}}_n^{\mathrm{p}} = \dot{v}_s^{\mathrm{p}} \boldsymbol{s} + \dot{v}_t^{\mathrm{p}} \boldsymbol{t} + \dot{v}_n^{\mathrm{p}} \boldsymbol{n} \tag{13}$$

with

$$\dot{\boldsymbol{v}}_i^{\mathrm{p}} = \dot{\boldsymbol{\lambda}}_i \partial_{\bar{\tau}} \Phi_i = \dot{\lambda}_i \operatorname{sign}(\bar{\boldsymbol{\tau}} \cdot \boldsymbol{i}) \boldsymbol{i} \tag{14}$$

as well as

$$\dot{\alpha}_i = \dot{\lambda}_i \partial_{R_i} \Phi_i = \dot{\lambda}_i \tag{15}$$

The Lagrangean multipliers $\dot{\lambda}_i$ of the underlying optimisation problem are restricted by the inequality constraint $\dot{\lambda}_i \geqslant 0, \Phi_i \dot{\lambda}_i = 0$ which takes the interpretation as loading and unloading condition for every direction. Consequently, $\dot{\lambda}_i$ is zero if no plastic displacement evolution takes place.

Exponential relations are chosen for the decoupled damage parameters d_i.

$$d_i = 1 - \exp(j_i[\mu_{0i} - \mu_i]) \tag{16}$$

The variable μ_i, accountable for the progression of damage in $\boldsymbol{i}$-direction, is computed according to

$$\mu_i = \max\{\bar{\mu}_i(\boldsymbol{v}^{\mathrm{e}}), \mu_{0i}\} \tag{17}$$

and the so-called damage driving force is given by

$$\bar{\mu}_i = -\partial_{d_i} \Psi = \frac{1}{2} \boldsymbol{v}^{\mathrm{e}} \cdot \boldsymbol{E}_i \cdot \boldsymbol{v}^{\mathrm{e}} \tag{18}$$

By Eq. (17), the actual elastic relative displacement energy is compared to the prior state what serves as a criterion whether damage proceeds or not. Please note that the values of the damage parameters either remain zero or increase monotonically. Being fixed material parameters, μ_{0i} is a damage threshold determining the initiation of damage and j_i represents the intensity of damage evolution.

3.2.1. Constitutive integrator

For the problem at hand, associated elastoplasticity [16] decoupled in the basis directions $\{\boldsymbol{s}, \boldsymbol{t}, \boldsymbol{n}\}$ is applied. Detailed background informations on the general theoretical formulations are reviewed in [17]. For a discrete time step $\Delta t = \overset{n+1}{t} - \overset{n}{t} > 0$, the implicit Euler Backward method is applied, namely

$$\begin{aligned} \overset{n+1}{\boldsymbol{v}}^{\mathrm{p}} &= \overset{n}{\boldsymbol{v}}^{\mathrm{p}} + \Delta t \left[\overset{n+1}{\dot{\boldsymbol{v}}}_s^{\mathrm{p}} + \overset{n+1}{\dot{\boldsymbol{v}}}_t^{\mathrm{p}} + \overset{n+1}{\dot{\boldsymbol{v}}}_n^{\mathrm{p}} \right] \\ &= \overset{n}{\boldsymbol{v}}^{\mathrm{p}} + \sum_i \overset{n+1}{\Delta\lambda}_i \operatorname{sign}\left(\overset{n+1}{\bar{\tau}}_i \right) \boldsymbol{i} \end{aligned} \tag{19}$$

The effective traction can, accordingly, be written as

$$\overset{n+1}{\bar{\boldsymbol{\tau}}} = \sum_i \left[\underbrace{\boldsymbol{E}_i \cdot \left[\overset{n+1}{\boldsymbol{v}} - \overset{n}{\boldsymbol{v}}^{\mathrm{p}} \right]}_{\bar{\tau}_i^{\mathrm{trial}}} - c_i \overset{n+1}{\Delta\lambda}_i \operatorname{sign}\left(\overset{n+1}{\bar{\tau}}_i \right) \boldsymbol{i} \right] \tag{20}$$

In what follows, transformations are explicitly shown for the $\boldsymbol{s}$-direction, whereas the transformations for the other directions can be performed following similar steps. The effective traction in $\boldsymbol{s}$-direction is given as:

$$\overset{n+1}{\bar{\boldsymbol{\tau}}}_s = \bar{\boldsymbol{\tau}}_s^{\mathrm{trial}} - c_s \overset{n+1}{\Delta\lambda}_s \operatorname{sign}\left(\overset{n+1}{\bar{\tau}}_s \right) \boldsymbol{s} \tag{21}$$

from which we conclude

$$\boldsymbol{s} = \boldsymbol{s}^{\mathrm{trial}}, \quad \overset{n+1}{\bar{\tau}}_s + c_s \overset{n+1}{\Delta\lambda}_s \operatorname{sign}\left(\overset{n+1}{\bar{\tau}}_s \right) = \bar{\tau}_s^{\mathrm{trial}} \tag{22}$$

Eq. $(22)_2$ is equivalent to

$$\frac{\bar{\tau}_s^{\mathrm{trial}}}{\left|\bar{\tau}_s^{\mathrm{trial}}\right|} \left|\bar{\tau}_s^{\mathrm{trial}}\right| = \frac{\overset{n+1}{\bar{\tau}}_s}{\left| \overset{n+1}{\bar{\tau}}_s \right|} \left| \overset{n+1}{\bar{\tau}}_s \right| + c_s \overset{n+1}{\Delta\lambda}_s \frac{\overset{n+1}{\bar{\tau}}_s}{\left| \overset{n+1}{\bar{\tau}}_s \right|} \tag{23}$$

Based on this relation together with $c_s \geqslant 0$ and $\overset{n+1}{\Delta\lambda}_s \geqslant 0$ one obtains after some transformations

$$\left| \overset{n+1}{\bar{\tau}}_s \right| = \left|\bar{\tau}_s^{\mathrm{trial}}\right| - c_s \overset{n+1}{\Delta\lambda}_s \quad \text{and} \quad \operatorname{sign}\left(\overset{n+1}{\bar{\tau}}_s \right) = \operatorname{sign}\left(\bar{\tau}_s^{\mathrm{trial}}\right) \tag{24}$$

During plastic evolution it is essential to satisfy the yield condition.

$$\overset{n+1}{\Phi}_s = \left| \overset{n+1}{\bar{\tau}}_s \right| - Y_{0s} + \overset{n+1}{R}_s = 0 \tag{25}$$

Furthermore, the Euler Backward method results in

$$\overset{n+1}{R}_s = R_s^{\mathrm{trial}} - H_s \overset{n+1}{\Delta\lambda}_s, \quad R_s^{\mathrm{trial}} = -H_s \overset{n}{\alpha}_s \tag{26}$$

Using Eqs. (24)–(26) renders the explicit update for the Lagrangean multiplier.

$$\overset{n+1}{\Delta\lambda}_s = \frac{\Phi_s^{\mathrm{trial}}}{c_s + H_s} \quad \text{with} \quad \Phi_s^{\mathrm{trial}} = \left|\bar{\tau}_s^{\mathrm{trial}}\right| - \left[Y_{0s} + R_s^{\mathrm{trial}}\right] \tag{27}$$

Combining Eqs. (21), (22), (24) and $(27)_1$, we end up with

$$\overset{n+1}{\bar{\boldsymbol{\tau}}}_s = \bar{\boldsymbol{\tau}}_s^{\mathrm{trial}} - \frac{\Phi_s^{\mathrm{trial}}}{1 + \frac{H_s}{c_s}} \operatorname{sign}\left(\bar{\tau}_s^{\mathrm{trial}}\right) \boldsymbol{s} \tag{28}$$

The effective traction vector update $\overset{n+1}{\bar{\boldsymbol{\tau}}}$ is then given by assembling terms of all directions, as well as the nominal traction vector update $\overset{n+1}{\bar{\boldsymbol{\tau}}}$.

$$\overset{n+1}{\bar{\boldsymbol{\tau}}} = \sum_i \overset{n+1}{\bar{\boldsymbol{\tau}}}_i, \quad \overset{n+1}{\boldsymbol{\tau}} = \sum_i \left(1 - \overset{n+1}{d}_i\right) \overset{n+1}{\bar{\boldsymbol{\tau}}}_i \tag{29}$$

Concerning the damage parameters d_i, one obtains the straightforward update

$$\overset{n+1}{d}_i = 1 - \exp\left(j_i \left[\mu_{0i} - \overset{n+1}{\mu}_i\right]\right) \tag{30}$$

with

$$\overset{n+1}{\mu}_i = \max\left\{\overset{n+1}{\bar{\mu}}_i \left(\overset{n+1}{\boldsymbol{v}}^{\mathrm{e}}\right), \overset{n}{\mu}_i, \mu_{0i}\right\} \tag{31}$$

and

$$\overset{n+1}{\bar{\mu}}_i = -\partial_{d_i} \overset{n+1}{\Psi} = \frac{1}{2} \overset{n+1}{\boldsymbol{v}}^{\mathrm{e}} \cdot \boldsymbol{E}_i \cdot \overset{n+1}{\boldsymbol{v}}^{\mathrm{e}} \tag{32}$$

If damage evolves, it is essential that

$$\overset{n+1}{\mu}_i = \overset{n+1}{\bar{\mu}}_i \left(\overset{n+1}{\boldsymbol{v}}^{\mathrm{e}}\right) \tag{33}$$

Note that the constitutive response of the proposed model is decoupled with respect to projections onto $\boldsymbol{s}$, $\boldsymbol{t}$ and $\boldsymbol{n}$. Otherwise local iterations have to be taken into account to solve for the Lagrangean multipliers from the set of non-linear equations. From the algorithmic point of view it would then not be significantly more expensive to additionally account for non-linear hardening effects.

3.2.2. Algorithmic tangent operator

When solving the obtained set of non-linear equations with a classical Newton scheme, the so-called algorithmic tangent

$$\boldsymbol{E}_{\mathrm{alg}}^{\mathrm{ep,dam}}\left(\overset{n+1}{\boldsymbol{v}}\right) = \partial_{\boldsymbol{v}} \overset{n+1}{\boldsymbol{\tau}} \tag{34}$$

is required to compute the global tangent matrix of the Finite Element code. This tensor-valued quantity is obtained from the derivation of the traction vector with respect to the relative displacement vector, see Eq. (34). Using Eqs. (9) and (34) gives

$$\begin{aligned}\partial_{\boldsymbol{v}} \overset{n+1}{\boldsymbol{\tau}} = \sum_i \Bigg[& \boldsymbol{E}_i \cdot \left[\boldsymbol{I} - \partial_{\boldsymbol{v}} \overset{n+1}{\boldsymbol{v}}^{\mathrm{p}}\right] - \overset{n+1}{d}_i \boldsymbol{E}_i - \left[\boldsymbol{E}_i \cdot \overset{n+1}{\boldsymbol{v}}\right] \otimes \partial_{\boldsymbol{v}} \overset{n+1}{d}_i \\ & + \overset{n+1}{d}_i \boldsymbol{E}_i \cdot \partial_{\boldsymbol{v}} \overset{n+1}{\boldsymbol{v}}^{\mathrm{p}} + \left[\boldsymbol{E}_i \cdot \overset{n+1}{\boldsymbol{v}}^{\mathrm{p}}\right] \otimes \partial_{\boldsymbol{v}} \overset{n+1}{d}_i \Bigg]\end{aligned} \tag{35}$$

To further develop Eq. (35), we observe from Eq. (19)

$$\partial_{\boldsymbol{v}} \overset{n+1}{\boldsymbol{v}}^{\mathrm{p}} = \sum_i \left[\overset{n+1}{\Delta\lambda}_i \partial_{\boldsymbol{v}} \left(\operatorname{sign}\left(\overset{n+1}{\bar{\tau}}_i\right)\boldsymbol{i}\right) + \left(\operatorname{sign}\left(\overset{n+1}{\bar{\tau}}_i\right)\boldsymbol{i}\right) \otimes \partial_{\boldsymbol{v}} \overset{n+1}{\Delta\lambda}_i\right] \tag{36}$$

Combining Eqs. (22), (24) and (36) renders for the $\boldsymbol{s}$-direction

$$\partial_{\boldsymbol{v}} \overset{n+1}{\Delta\lambda}_s = \partial_{\boldsymbol{v}} \frac{\left|\bar{\tau}_s^{\mathrm{trial}}\right|}{c_s + H_s} = \partial_{\boldsymbol{v}} \frac{\left|\left[\boldsymbol{E} \cdot \left[\overset{n+1}{\boldsymbol{v}} - \overset{n}{\boldsymbol{v}}^{\mathrm{p}}\right]\right] \cdot \boldsymbol{s}\right|}{c_s + H_s} = \frac{\operatorname{sign}\left(\bar{\tau}_s^{\mathrm{trial}}\right)}{1 + \frac{H_s}{c_s}} \boldsymbol{s} \tag{37}$$

as well as

$$\partial_{\boldsymbol{v}}\left(\operatorname{sign}\left(\bar{\tau}_s^{\mathrm{trial}}\right)\boldsymbol{s}\right) = \partial_{\boldsymbol{v}} \frac{\bar{\boldsymbol{\tau}}_s^{\mathrm{trial}}}{\left\|\bar{\boldsymbol{\tau}}_s^{\mathrm{trial}}\right\|} = \partial_{\boldsymbol{v}} \boldsymbol{s} = \boldsymbol{0} \tag{38}$$

For the other directions, similar steps are proceeded. Considering this and Eqs. (37), (38) and (36) gives

$$\partial_{\boldsymbol{v}} \overset{n+1}{\boldsymbol{v}}^{\mathrm{p}} = \sum_i \frac{1}{1 + \frac{H_i}{c_i}} \boldsymbol{i} \otimes \boldsymbol{i} \tag{39}$$

Making use of the chain rule, further terms occurring in, e.g., Eq. (35) are identified.

$$\partial_{\boldsymbol{v}} \overset{n+1}{d}_s = \partial_{\mu_s} \overset{n+1}{d}_s \, \partial_{\bar{\mu}_s} \overset{n+1}{\mu}_s \, \partial_{\boldsymbol{v}} \overset{n+1}{\bar{\mu}}_s \tag{40}$$

with

$$\partial_{\mu_s} \overset{n+1}{d}_s = j_s \exp\left(j_s \left[\mu_{0s} - \overset{n+1}{\mu}_s\right]\right) \tag{41}$$

and

$$\partial_{\bar{\mu}_s} \overset{n+1}{\mu}_s = \begin{cases} 1 & \text{if } \overset{n+1}{d}_s - \overset{n}{d}_s > 0 \\ 0 & \text{else} \end{cases} \tag{42}$$

In order to derive the format of a non-elastic algorithmic tangent operator, we next place emphasis on the case where damage evolves ($\partial_{\bar{\mu}_s} \overset{n+1}{\mu}_s = 1$). Combining the third factor in Eq. (40) with Eq. (39) renders for inelastic loading

$$\begin{aligned}\partial_{\boldsymbol{v}} \overset{n+1}{\bar{\mu}}_s &= \frac{1}{2} \partial_{\boldsymbol{v}} \left[\left[\overset{n+1}{\boldsymbol{v}} - \overset{n+1}{\boldsymbol{v}}^{\mathrm{p}}\right] \cdot \boldsymbol{E}_s \cdot \left[\overset{n+1}{\boldsymbol{v}} - \overset{n+1}{\boldsymbol{v}}^{\mathrm{p}}\right]\right] \\ &= \left[1 - \frac{1}{1 + \frac{H_s}{c_s}}\right] \boldsymbol{E}_s \cdot \overset{n+1}{\boldsymbol{v}}^{\mathrm{e}}\end{aligned} \tag{43}$$

Application of Eqs. (41)–(43) now enables to rewrite Eq. (40) as

$$\partial_{\boldsymbol{v}} \overset{n+1}{d}_s = j_s \exp\left(j_s \left[\mu_{0s} - \overset{n+1}{\mu}_s\right]\right) \left[1 - \frac{1}{1 + \frac{H_s}{c_s}}\right] \boldsymbol{E}_s \cdot \overset{n+1}{\boldsymbol{v}}^{\mathrm{e}} \tag{44}$$

Inserting these results and Eq. (39) into Eqs. (35) and (34), respectively, renders

$$\begin{aligned}\boldsymbol{E}_{alg}^{\mathrm{ep,dam}} = \sum_i \Bigg[& \left[\left[1 - \overset{n+1}{d}_i\right] \boldsymbol{E}_i \right. \\ & \left. - \overset{n+1}{\bar{\boldsymbol{\tau}}}_i \otimes \overset{n+1}{\bar{\boldsymbol{\tau}}}_i \, j_i \exp\left(j_i \left[\mu_{0i} - \overset{n+1}{\mu}_i\right]\right)\right] \left[1 - \frac{1}{1 + \frac{H_i}{c_i}}\right]\Bigg]\end{aligned} \tag{45}$$

4. Finite element method

Embedded between standard continuum elements, interface elements have no numerical width. They are designed to model material interfaces and do not possess typical deficiencies (as for instance ill-conditioned tangent operators) of continuum elements with a very high ratio of length and height. Moreover, when for example laminar welded shear tension tests are investigated, the zone of

delamination is known a priori. As such, interface elements combined with appropriate material models can systematically be used to model zones which are expected to delaminate.

In what follows, a summary of the used interface formulation embedded into a non-linear Finite Element code is highlighted. All considerations are reviewed for a two-dimensional problem; the three-dimensional case can be deduced straightforwardly.

4.1. Element level

The virtual internal work of an interface element is given by:

$$\delta \mathscr{W}_{\Gamma_e} = \int_{\Gamma_e} \delta \boldsymbol{v} \cdot \boldsymbol{\tau}(\boldsymbol{v}) \, \mathrm{d}S \tag{46}$$

To model interfaces in three dimensions, two-dimensional interface elements are used. Accordingly, one-dimensional interface elements are necessary for interfaces in two-dimensional domains. To assimilate the virtual internal work in a global Finite Element context, the relative displacements $\boldsymbol{v}$ between the upper and the lower element can be approximated by linear shape functions (see also Fig. 7)

$$\boldsymbol{N} = [N_{\mathrm{I}}, N_{\mathrm{II}}] = [0.5(1-\xi), 0.5(1+\xi)] \tag{47}$$

for $\xi \in [-1, 1]$ and can be expressed by the absolute displacements of the surrounding elements. Absolute displacements are relevant concerning the surrounding elements. The displacement vector of the ambient nodes is defined with respect to a fixed orthonormal base system $\{\boldsymbol{e}_x, \boldsymbol{e}_y, \boldsymbol{e}_z\}$ as

$$\boldsymbol{d}_e = [u_x^1, u_y^1, u_x^2, u_y^2, u_x^3, u_y^3, u_x^4, u_y^4]^t \tag{48}$$

The correlation between relative displacements $\boldsymbol{v}^h$ and absolute displacements $\boldsymbol{d}_e$ is then introduced via

$$\boldsymbol{a}^h = \boldsymbol{H} \cdot \boldsymbol{d}_e, \quad \boldsymbol{v}^h = \boldsymbol{L} \cdot \boldsymbol{a}^h, \quad \boldsymbol{v}^h = \underbrace{\boldsymbol{L} \cdot \boldsymbol{H}}_{\boldsymbol{B}} \cdot \boldsymbol{d}_e \tag{49}$$

so that $\boldsymbol{a}^h = [a_x^u, a_x^l, a_y^u, a_y^l]^t$ contains the linear approximation of upper and lower displacements depending on ξ and related to the displacement vector by the matrix

$$\boldsymbol{H} = \begin{bmatrix} 0 & 0 & 0 & 0 & N_{\mathrm{I}} & 0 & N_{\mathrm{II}} & 0 \\ N_{\mathrm{I}} & 0 & N_{\mathrm{II}} & 0 & 0 & 0 & 0 & 0 \\ 0 & 0 & 0 & 0 & 0 & N_{\mathrm{I}} & 0 & N_{\mathrm{II}} \\ 0 & N_{\mathrm{I}} & 0 & N_{\mathrm{II}} & 0 & 0 & 0 & 0 \end{bmatrix} \tag{50}$$

The approximated relative displacement vector $\boldsymbol{v}$ is determined by multiplication with the matrix

$$\boldsymbol{L} = \begin{bmatrix} 1 & -1 & 0 & 0 \\ 0 & 0 & 1 & -1 \end{bmatrix} \tag{51}$$

In conclusion, the matrix $\boldsymbol{B}$ (see Eq. $(49)_3$) takes the representation

$$\boldsymbol{B} = \begin{bmatrix} -N_{\mathrm{I}} & 0 & -N_{\mathrm{II}} & 0 & N_{\mathrm{I}} & 0 & N_{\mathrm{II}} & 0 \\ 0 & -N_{\mathrm{I}} & 0 & -N_{\mathrm{II}} & 0 & N_{\mathrm{I}} & 0 & N_{\mathrm{II}} \end{bmatrix} \tag{52}$$

With these relations in hand, Eq. (46) is rewritten in the domain of one interface element.

$$\delta \mathscr{W}^h_{\Gamma^e} = \int_{\Gamma^e} \delta \boldsymbol{d}_e \cdot \boldsymbol{B}^t \cdot \boldsymbol{\tau}(\boldsymbol{v}^h) \, \mathrm{d}S \tag{53}$$

Linearisation renders

$$\Delta\delta \mathscr{W}^h_{\Gamma^e} = \int_{\Gamma^e} \delta \boldsymbol{d}_e \cdot \boldsymbol{B}^t \cdot \boldsymbol{E}^{\mathrm{ep,dam}}_{\mathrm{alg}} \cdot \boldsymbol{B} \cdot \Delta \boldsymbol{d}_e \, \mathrm{d}S \tag{54}$$

From this, the internal force vector $\boldsymbol{S}^e$ and the tangent matrix $\boldsymbol{K}^e$ for an interface element can be derived. Simultaneously, an integral transformation with respect to a reference domain spanned by ξ is performed.

$$\boldsymbol{S}^e = \int_{-1}^{1} \boldsymbol{B}^t \cdot {}^{n+1}\boldsymbol{\tau}(\boldsymbol{v}^h) \left\| \frac{\partial \boldsymbol{x}(\xi)}{\partial \xi} \right\| \mathrm{d}\xi \tag{55}$$

$$\boldsymbol{K}^e = \int_{-1}^{1} \boldsymbol{B}^t \cdot \boldsymbol{E}_{\mathrm{alg}} \cdot \boldsymbol{B} \left\| \frac{\partial \boldsymbol{x}(\xi)}{\partial \xi} \right\| \mathrm{d}\xi \tag{56}$$

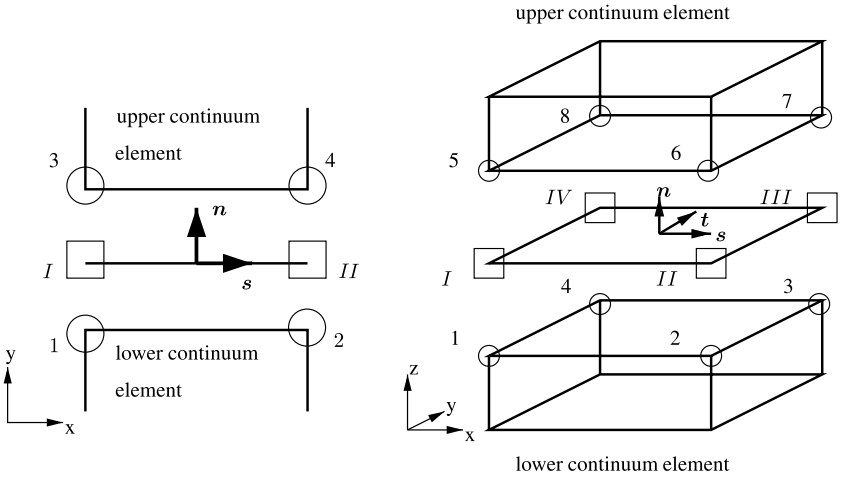

Fig. 7. Schematic sketch of a one-dimensional (left) and two-dimensional (right) interface element.

Here, $\boldsymbol{x}(\xi) = \boldsymbol{x}_{\mathrm{I}} N_{\mathrm{I}} + \boldsymbol{x}_{\mathrm{II}} N_{\mathrm{II}}$ is the parametrisation of the interface element with respect to Eq. (47). The quantities $\boldsymbol{x}_{\mathrm{I}}$ and $\boldsymbol{x}_{\mathrm{II}}$ thereby represent the interface node position vectors, pointing to the average positions of nodes 1, 3 and 2, 4, respectively (compare Fig. 7). To perform the integration of Eq. (56) numerically, a Gauss integration with two integration points is applied.

4.2. Global level

Body forces being neglected, the weak form in integral representation for the two-dimensional domain of interest reads

$$\int_{\mathscr{B}} \boldsymbol{\varepsilon}(\delta\boldsymbol{u}) : \boldsymbol{\sigma}(\boldsymbol{u})\,\mathrm{d}A + \int_{\Gamma} \delta\boldsymbol{v} \cdot \boldsymbol{\tau}(\boldsymbol{v})\,\mathrm{d}S = \int_{\partial\mathscr{B}} \delta\boldsymbol{u} \cdot \overset{*}{\boldsymbol{t}}\,\mathrm{d}S \qquad (57)$$

with $\boldsymbol{\varepsilon}$ being the strains, $\boldsymbol{\sigma}$ being the stresses, $\boldsymbol{u}$ being the element displacement vector, $\boldsymbol{v}$ being the relative displacements, $\boldsymbol{\tau}$ being the traction vector in the interface, $\overset{*}{\boldsymbol{t}}$ being the prescribed tractions, $\mathscr{B}$ being the interface-surrounding domain and Γ being the domain of the interface.

A Finite Element based discretisation renders, by utilising an assembly algorithm, the global stiffness matrix of the current iteration step. The Finite Element mesh data is created according to the three-dimensional geometry of the experimentally investigated shear tension test. The numerical computations are based on eight-noded linear continuum elements for the surrounding steel substrates. Their constitutive behaviour is chosen as geometrically linear elastoplasticity with linear hardening effects.

5. Results and discussion

As can be seen in Fig. 8, the experimentally obtained macroscopic force–displacement-curve is nicely reproduced by the simulation, whereby a model with 5208 elements has been applied. The chosen material parameters for the steel substrate are: Young's modulus 166900 MPa, Poisson ratio 0.3, yield stress 140.3 MPa and hardening modulus 95 MPa; while suitable material parameters for the interface are: $c_s = c_t = 35211$ MPa/m, $c_n = 100000$ MPa/m, $Y_{0s} = Y_{0t} = Y_{0n} = 21.5$ MPa/m, $H_s = H_t = H_n = 150$ MPa/m, $\mu_{0s} = \mu_{0t} = \mu_{0n} = 0.0075$ MPa m, and $j_s = j_t = j_n = 47.5\ (\mathrm{MPa\ m})^{-1}$.

Three zones can be identified from Fig. 8: an elastic zone, an elastoplastic zone, and a damaged zone. According to the appropriate model and set of material parameters, the simulated force–displacement-curve fits to the experimental data. The first zone is given by an elastic straight line. In the second zone, beginning at a force of approximately 4500 N, elastoplastic hardening effects in both the bulk and the interface occur. Identifying the third zone which begins at approximately 7000 N, a softening behaviour of the specimen can be seen due to interfacial damage activity, followed by complete failure. The sharpness of this last zone shows a brittle behaviour subsequent to the elastoplastic zone. Since integral-type-data is essentially one-dimensional, local analyses using Electronic Speckle Pattern Interferometry (ESPI) are additionally performed. Based on two-dimensional data fields, comparisons between ESPI and numerical simulations constitute an important part of the validation procedure so that the set of material parameters is not determined from purely one-dimensional measurements. To be specific, using different material parameters, similar one-dimensional force–displacement curves can be generated. The optical analyses with ESPI shown here are applied to the narrow side of the specimen and are supported during the entire loading history. Here, Figs. 9–11 are referred to loadstep 25/30. Concerning simulation details, the discretisation of the

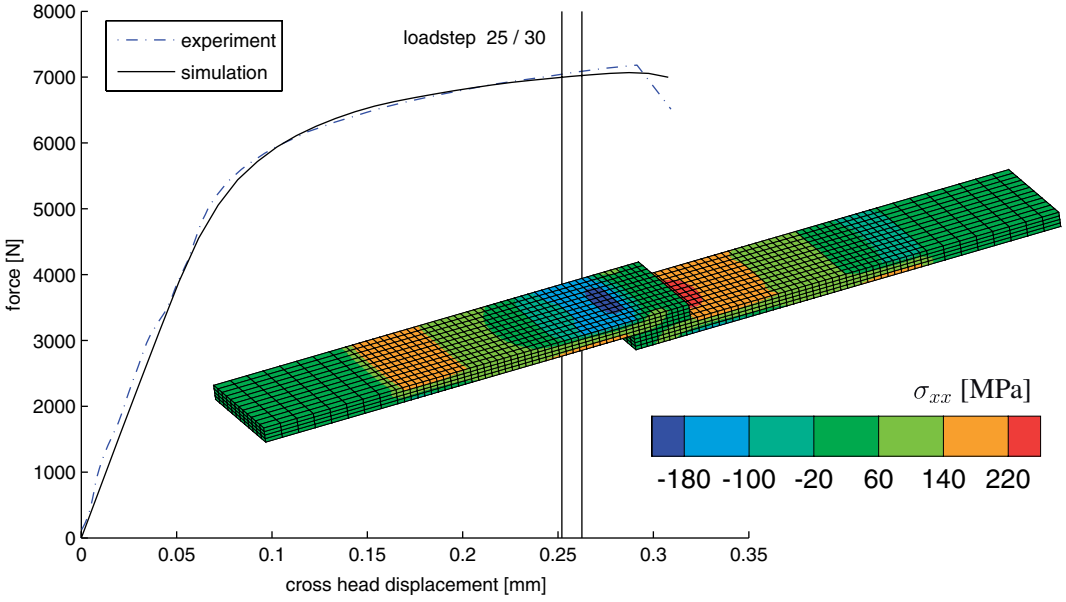

Fig. 8. Force–displacement-curve of a thermal impact welded single lap tensile specimen (left) and normal stress in loading direction σ_{xx}, loadstep 25/30 (right).

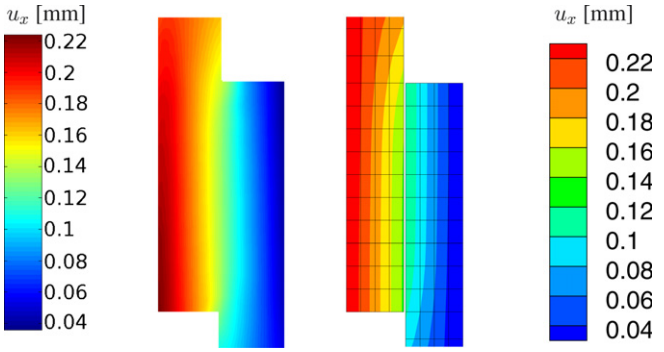

Fig. 9. ESPI image of a displacement offset in loading direction (left) and corresponding simulation loadstep 25/30 (right).

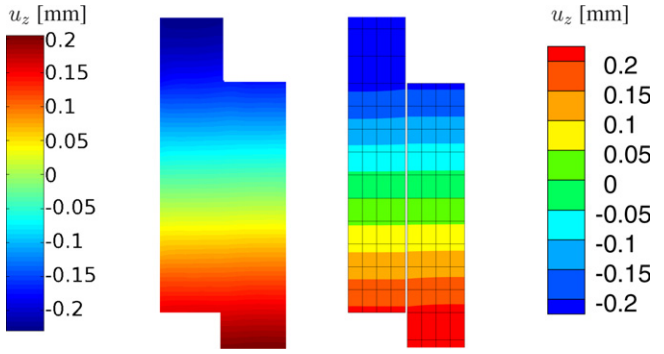

Fig. 10. ESPI image of a displacement offset in out-of-plane direction (left) and corresponding simulation loadstep 25/30 (right).

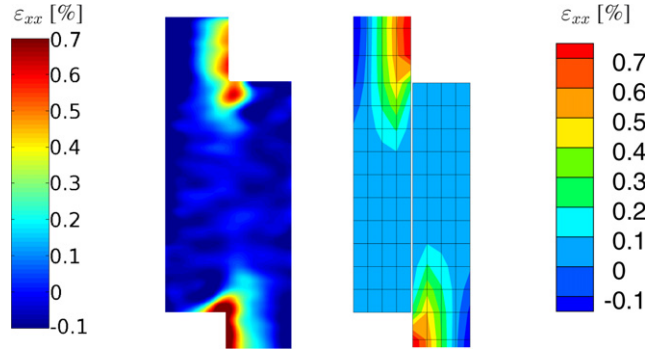

Fig. 11. ESPI image based strains in loading direction (left) and corresponding simulation loadstep 25/30 (right).

mesh is throughout shown in the undeformed configuration. Note that the interface itself is not displayed in the results because of its dimensional deficiency. Placing emphasis on Fig. 9, one observes quantitative agreements between experimental and simulation results concerning deformations in loading direction. In Fig. 10, the so-called out-of-plane deformation (bending displacement) is shown. By analogy with Fig. 9, good quantitative similarities are observed. Finally, strain distributions in loading direction are compared in Fig. 11. Apart from the distinct qualitative similarity of the ESPI image and the simulation, quantities are in good agreement. Note that the quality of the ESPI result is influenced by smoothing data, and by the fact that the specimen turns out of the fixed observation frame which is shown here, due to the torque induced by the geometry. Besides this, a possible reason for differences may be that in the process of TIW, PEEK leaks out of the interfacial zone and accumulates at the corners, which is not accounted for in the simulation. With the computations, maximum strains occur slightly shifted compared to the ESPI image. This can possibly be traced back on the size of the mesh.

6. Conclusions

By using interfacial elastoplasticity with Lemaitre-type-damage, the phenomenological simulation of global force–displacement-curves has successfully been captured. One-dimensional integral-type data has successfully been modelled. Two-dimensional data, especially local displacements, have quantitatively been captured. Good qualitative and, up to some degree, also quantitative similarities occur when comparing local strains in loading direction. Nevertheless, at the present stage, investigations still inhere the need of further efforts. In this context, advanced elaborations on the identification of material parameters [18,19] are planned for the future. In addition, more realistic constitutive laws for the steel substrates such as multiplicative elastoplasticity [20–22] could be implemented. Also further modifications and refinements of the FE-mesh could be helpful, even though on the expense of computational costs. Additionally, other experimental methods to produce two-dimensional data will be consulted. By proceeding along these lines, it is expected that all experimental measurements can even better be captured by the developed simulation tool.

Acknowledgements

The authors thank the German Research Foundation (DFG) for financial support within the DFG-Research Unit 524 Manufacturing, Characterisation and Simulation of Welded Lightweight Structures of Metal/Fibre-Reinforced Polymer Composites (DFG STE 544/21-1/DFG FR 675/44-1/DFG RE 1717/1-1) at the University of Kaiserslautern.

References

[1] A.M. Häger, K. Friedrich, Aufbau und Eigenschaften von Polymer-Verbundwerkstoffen für reibungs- und verschleissbelastete Bauteile, in: W.J. Bartz (Ed.), 10th International Colloquium: Tribology – Solving Friction and Wear Problems, vol. 1, Techn. Akademie Esslingen, Ostfildern, 1996, pp. 561–569.
[2] K. Friedrich, Z. Lu, A.M. Häger, Theor. Appl. Fract. Mech. 19 (1993) 1–11.
[3] H.P. Beringer, G. Heinke, E. Strickle, Materialwissenschaften und Werkstofftechnik 22 (1991) 168–173.
[4] S.A.R. Naga, Effect of glass fibre content on the frictional behaviour of glass fibre reinforced polyamide 66. Tribologie 2000, 8. Int.

Kolloquium, Technische Akademie Esslingen, 1992, pp. 25.7.1–25.7.6.
[5] G.W. Ehrenstein, G. Riedel, P. Trawiel, Praxis der Thermischen Analyse von Kunststoffen, Carl Hanser Verlag, München, 2003.
[6] F. Oster, F. Haupert, K. Friedrich, Tribologie-Fachtagung Göttingen (2000) 31/1–31/10.
[7] G. Krüger, U. Meyer, Adhäsion – Kleben & Dichten 42 (1998) 31–34.
[8] G. Cloud, Optical Methods of Engineering Analysis, Cambridge, 1995.
[9] L. Yang, A. Ettemeyer, Opt. Eng. SPIE 42 (2003) 5.
[10] J.C.J. Schellekens, Computational strategies for composite structures – Dissertation, Technische Universiteit Delft, The Netherlands, 1992.
[11] P. Steinmann, P. Betsch, Int. J. Solids Struct. 37 (2000) 4061–4082.
[12] K. Willam, I. Rhee, B. Shing, Comput. Methods Appl. Mech. Eng. 193 (2004) 3327–3350.
[13] J. Lemaitre, A Course on Damage Mechanics, Springer, 1992.
[14] R. Larsson, N.E. Jansson, Int. J. Numer. Methods Eng. 54 (2002) 473–497.
[15] N.E. Jansson, R. Larsson, Compos. Struct. 53 (2001) 409–417.
[16] C. Miehe, J. Schröder, Arch. Appl. Mech. 64 (1994) 267–285.
[17] J.C. Simo, T.J.R. Hughes, Computational Inelasticity, Springer, 1998.
[18] R. Mahnken, E. Stein, Comput. Methods Appl. Mech. Eng. 136 (1996) 225–258.
[19] R. Mahnken, E. Stein, Comput. Methods Appl. Mech. Eng. 147 (1997) 17–39.
[20] J. Schröder, F. Gruttmann, J. Löblein, Comput. Mech. 30 (2002) 48–64.
[21] A. Menzel, M. Ekh, K. Runesson, P. Steinmann, Int. J. Plasticity 21 (2005) 397–434.
[22] P. Steinmann, C. Miehe, E. Stein, Comput. Mech. 13 (1994) 458–474.

Please cite this article in press as: J. Utzinger et al., Comput. Mater. Sci. (2007), doi:10.1016/j.commatsci.2007.04.015